HOSTED BY
ELSEVIER
Available online at www.sciencedirect.com
ScienceDirect
Soils and Foundations 60 (2020) 989–1000
www.elsevier.com/locate/sandf

Comparison of UBCSAND and Hypoplastic soil model predictions using the Material Point Method

Shreyas Giridharan [a,*], Sujith Gowda [a], Dieter F.E. Stolle [b], Christian Moormann [a]

[a] *Institute of Geotechnical Engineering, University of Stuttgart, Pfaffenwaldring 35, 70569 Stuttgart, Germany*
[b] *Department of Civil Engineering, McMaster University, 1280 Main Street West, Hamilton, Ontario, Canada*

Received 3 September 2019; received in revised form 2 June 2020; accepted 14 June 2020
Available online 9 August 2020

Abstract

Liquefaction effects predicted by implementing two well-known constitutive models for sandy soils are compared; i.e., the Hypoplastic soil model (HPS) and the UBCSAND model. To numerically simulate dynamic loading, the Convected Particle Domain Interpolation (*CPDI*) method, an advanced Material Point Method (*MPM*), is employed within a multi-phase framework. The numerical results from the UBCSAND model are compared against published experimental data. A comparison between the performance of UBCSAND and HPS model is presented by calibrating the former's constitutive behaviour for Berlin sand to that of the HPS model. The shake table test performed at Rensselaer Polytechnic Institute is numerically simulated and results are compared against the published experimental data. Good agreement between the experiment and the numerical calculation is obtained. Thereafter, models are employed to numerically simulate a driven pile installation. The results from both models are compared against published experimental data. The multi-phase *CPDI* formulation is shown to be capable of reproducing liquefaction for the the pile driving example.

Keywords: MPM; CPDI; Liquefaction; UBCSAND; Hypoplastic Sand

1. Introduction

Liquefaction takes place due to the accumulation of excess pore pressure in loose saturated sandy soils subject to cyclic loading. This phenomenon is often accompanied by large ground subsidence that serves as a trigger for damage to structures. Major earthquakes that occurred in the past such as the Niigata earthquake of 1964, Alaskan earthquake of 1964, Loma Prieta earthquake of 1989, or Hyogoken-Nambu earthquake of 1995 have demonstrated the destructive effects of soil liquefaction.

Seismic analyses based on the finite element method allow an assessment of the liquefaction potential of soil taking more realistically into account the nature of loading, and the generation and dissipation of excess pore pressure. Such analyses are often time-consuming owing to the high computational effort necessary to perform the simulations. Besides, the constitutive models that are employed, often require a large number of parameters that must be calibrated to obtain reasonable pore pressure generation estimations. For this reason, simplified methods are often popular in engineering practice for assessing the liquefaction risk during the preliminary design stage. The most popular simplified methods that are in use, include: (a) those based on cyclic shear stresses generated in the soil (Robertson and Wride, 1998), (b) probabilistic methods (Juang et al., 2001), and (c) energy-based methods (Berrill and Davis, 1985). If the liquefaction risk is high, a detailed finite element analysis can be performed to better estimate the excess pore pressures and the resulting ground displacement.

Peer review under responsibility of The Japanese Geotechnical Society.
* Corresponding author.
E-mail address: shreyas.giridharan@igs.uni-stuttgart.de (S. Giridharan).

https://doi.org/10.1016/j.sandf.2020.06.001
0038-0806/

In spite of the drawbacks, finite element analyses remain attractive, in part due to their capability to capture the physics behind liquefaction, as well as it being ubiquitous. The accuracy of a solution depends however on the scheme adopted for the analysis, the constitutive model employed and the quality of the calibrated parameters. In addition to a constitutive model that is capable of capturing hardening, strength reduction and the hysteretic response of soil, the finite element approach is required to numerically simulate the complex dynamic behavior of saturated soils. The approach must also be capable modeling the two-phase behavior of soils accurately (Van Esch et al., 2011) and also capture the large deformation consequences that accompany post-liquefaction.

Several commercial finite element codes for modeling soil-structure interaction are available. A common drawback of most commercial codes is their inability to properly capture the ensuing large deformations adequately within a Lagrangian framework. Furthermore, classical finite element analyses often become numerically unstable when large deformations develop owing to mesh entanglement. Although this drawback can be overcome by re-meshing, the computational cost can be high. Alternative methods such as the Coupled Eulerian-Lagrangian (*CEL*) have been developed, in which zones of large deformation are treated by employing an Eulerian description locally. In more recent years, the Material Point Method (*MPM*) has become popular. It combines the advantages of both Eulerian and Lagrangian frameworks for capturing large deformation effects. To this end, a two-phase Convected Particle Domain Interpolation (*CPDI*) procedure (Sadeghirad et al., 2011), an advancement to the classical Material Point Method (*MPM*), has been implemented in this study.

Two constitutive models were chosen for this study: (a) a hypo-plasticity soil model with small-strain stiffness, which is referred to as the HPS herein (Niemunis and Herle, 1997); and (b) the UBCSAND model (Naesgaard, 2011). The HPS model has been successfully used to model liquefaction for numerical element tests in the work of (Tsegaye et al., 2010). It has also been applied to other complex geotechnical problems involving saturated soil with success (Moormann et al., 2018). This is attributed to the model being versatile in its ability to model both static and cyclic loads and its availability as an add-on UMAT file for various commercial finite element packages. UBCSAND is an elastoplastic model that is also capable of capturing the liquefaction effects (Puebla et al., 1997). Although there are commercial implementations of UBCSAND in PLAXIS and in FLAC, the corresponding dynamic linked libraries are at times incompatible with in-house codes or require permission for their use. Therefore, the model reported in detail in (Naesgaard, 2011) was re-written in FORTRAN and implemented in the in-house *CPDI* code for this study.

This paper begins with a brief overview of the multi-phase formulation and constitutive laws, followed by a description of the *CPDI* method, including a contact law that is required to accommodate the interaction between a soil and a pile. To test the implementation of the constitutive model in the two-phase *CPDI* code, the well-known case study (Byrne et al., 2004) of a shake table test is modelled. Predictions from the numerical simulations are compared with the published experimental results to demonstrate the capability of UBCSAND together with the *CPDI* code to capture the measured results. Some of the results have been published in (Giridharan et al., 2019) but are significantly extended in this paper. The performance of UBCSAND is also compared to that of HPS for the shake table setup test. The *CPDI* model is applied thereafter to simulate a vibratory-driven-pile with the results from both soil models being compared against published experimental results (Remspecher et al., 2018). Through this comparison, it is shown that the *CPDI* tool is capable of capturing, not only the liquefaction of the benchmark, but also of a pile installation. The paper ends with concluding remarks.

2. Overview of model

An extensive literature survey on the finite element implementation of the two-phase problems, including seismically-induced liquefaction, is presented in Reference (Zienkiewicz et al., 1990). The governing equations for both fully saturated and unsaturated behavior are provided. It has been shown in (Van Esch et al., 2011) that the velocity–pressure ($v-p$) formulation can only capture dynamic responses of a limited number of two-phase problems. A more general solid and water velocity ($v-w$) formulation is for this reason adopted in this paper. A detailed explanation is presented in (Zienkiewicz and Shiomi, 1984, Van Esch et al., 2011). The capability of the $v-w$ formulation to more adequately capture the physical response of saturated soil under dynamic loading is attributed to the momentum balance of both the mixture and fluid being taken into account. The $v-w$ formulation also provides an identical physically-based mapping of both mixture and water momentum between the particles and grid-points within the framework of the Material Point Method. There is no distinction drawn in the algorithm adopted for calculating the velocities of the water and of the mixture. The updating of particle location depends only on the solid phase displacements. In this formulation, velocities of each phase are calculated at the nodes as primary variables, whereas the water pressure and effective stresses are calculated at the Gauss points (in the case of *FEM*) or for the particles (considering *MPM*). The respective momentum equations for the water phase and the mixture are given by,

$$\rho_w \frac{dw_i}{dt} = \frac{\partial p}{\partial x_i} + \rho_w g_i - \frac{n \rho_w g}{k} (w_i - v_i), \tag{1}$$

$$(1-n)\rho_s \frac{\partial v_i}{\partial t} = -n \rho_w \frac{\partial w_i}{\partial t} + \frac{\partial \sigma_{ij}}{\partial x_j} + \rho_{sat} g_i, \tag{2}$$

where, ρ_w, ρ_s and ρ_{sat} are the water, solid and saturated soil densities, respectively. The indices i, j refer to the x- and y-directions, respectively, g_i denotes the gravitational acceleration in the x_j-direction, and w_i and v_i are the velocities of fluid and solid phases, respectively. The variable σ_{ij} refers to the total stress, k is the hydraulic conductivity of soil and n denotes the porosity. Equation (1) contains the drag term, corresponding to Darcy's law. The rate of change of pore pressure is calculated by using the mass balance equation that serves as the constitutive law for the water, i.e.,

$$\frac{dp}{dt} = \frac{K_w}{n}\left[(1-n)\,\frac{\partial v_i}{\partial x_i} + n\,\frac{\partial w_i}{\partial x_i}\right], \tag{3}$$

with K_w being the bulk modulus of the water phase. Total stress in the soil is related to the effective stress σ'_{ij} and pore pressure p by

$$\sigma_{ij} = \sigma'_{ij} + p\,\delta_{ij}, \tag{4}$$

in which the effective stress, as usual, is obtained from the constitutive model for the soil. To aid in numerical stability, the fluid- and mixture-strains are smoothened during each computational step via the relation:

$$\bar{\varepsilon} = \frac{\sum_e \varepsilon\, M_p\, S_i}{\sum_e M_p\, S_i}, \tag{5}$$

where, $\bar{\varepsilon}$, ε, M_p, S_i are the smoothened strains, computed strains, particle mass and grid basis functions, respectively.

3. UBCSAND model

This section provides a brief description of the UBCSAND model. For details and precise definitions of variables, the reader is referred to Reference (Puebla, 1999).

Elastic response - The elastic response of the constitutive model is assumed to be isotropic, in which the shear modulus G^e, and the bulk modulus B^e are given by relations,

$$G^e = K^e_G\, P_a\, \left(\frac{\sigma'}{P_a}\right)^{n_e}, \tag{6}$$

$$B^e = K^e_B\, P_a\, \left(\frac{\sigma'}{P_a}\right)^{m_e}. \tag{7}$$

The parameter P_a is the atmospheric pressure, assumed to be 100 kPa for all simulations, σ' denotes the mean effective stress, and n_e and m_e are elastic exponents that vary between 0.4 and 0.6. K^e_G and K^e_B are the shear and bulk modulus numbers, respectively.

Plastic response - Plastic strain rates are controlled by the yield loci, which are assumed to be radial lines, starting at the origin in stress space. For first-time loading, the yield locus is defined by the current stress state of the soil. As the shear stress (τ) increases, the stress-ratio (η), given by ($\eta = \frac{\tau}{\sigma'}$), increases as well, activating the primary yield surface according to an isotropic hardening rule, where the hardening law is given by the relation

$$\eta_d = \frac{\gamma^{ps}}{\left[\left(\frac{\sigma'}{G^e}\right) + \left(\frac{\gamma^{ps} R_f}{\eta}\right)\right]}, \tag{8}$$

where, γ^{ps} is the plastic shear strain, R_f is the failure ratio. As a result, the yield surface is dragged to the new location, expanding the elastic zone of the model. During this process, both shear and volumetric plastic strains develop. Unloading, which is elastic in nature, deactivates the primary yield surface. A Mohr-Coulomb type failure function is assumed to determine the ultimate strength and state of stress achievable in this model (Naesgaard, 2011); i.e.,

$$f_f = \sigma'_1 - \sigma'_3\, N_{\phi_f} + 2\,c\,\sqrt{N_{\phi_f}}, \tag{9}$$

with σ'_1 and σ'_3 being the effective major and minor principal stresses, respectively. The parameter c is the cohesion and N_{ϕ_f} is given by the relation,

$$N_{\phi_f} = \frac{1 + sin(\phi_f)}{1 - sin(\phi_f)}, \tag{10}$$

in which ϕ_f is the peak friction angle. The flow rule assumes,

$$\frac{d\epsilon^p_v}{d\gamma^p_s} = -tan(\psi), \tag{11}$$

with ϵ^p_v representing the plastic volumetric strain, γ^p_s being the plastic shear strains and ψ referring to the dilatation angle. The friction angle corresponding to constant volume (ϕ_{cv}) and the dilatation angle are related by the relation,

$$sin(\phi_{cv}) = \eta - sin(\psi), \tag{12}$$

where, η is the developed stress ratio. Additionally, η is bound by the rule $\eta \leq sin(\phi_f)$.

In addition to the previously mentioned physical parameters, additional variables $hfac_1$ to $hfac_6$, are introduced to control plasticity hardening and hysteresis loop details. They modify: number of cycles to trigger liquefaction; shape of pore pressure rise with the number of cycles; dilatation characteristics to control the post-trigger response; secondary dilatation characteristics after triggering; and failure envelope pull-down below ϕ_{pt} upon unloading. For specific details, the reader is referred to (Naesgaard, 2011).

4. HPS model

Although the UBCSAND model is capable of capturing the development of liquefaction associated with dynamic loading, the HPS model enjoys the advantage of being widely available for use in commercial finite element software. The values for soil parameters are available for a large number of soil types and calibration routines are available that aid in simplifying the process of parameter calibration. From a soil mechanics point of view, the HPS model can also take into account effects associated with changes in void ratio. The results of undrained triaxial compression and simple cyclic shear tests using the HPS

model are presented in the work of (Tsegaye et al., 2010). An example in which the HPS model is used to numerically simulate a tunnel response under seismic loading is presented in (Hleibieh et al., 2014). The HPS constitutive description has also been applied for liquefaction mitigation in (Nagula and Grabe, 2017). The HPS proposed by Von Wolffersdorff (1996) and extended to include the intergranular strain concept (Niemunis and Herle, 1997) is adopted in this study. The model incorporates the critical state concept in soil mechanics, as well as the possibility of updating the material stiffness and density, which depend on the stress level. Given function $\boldsymbol{H}$, the hypoplastic equation is represented as $\dot{\sigma} = \boldsymbol{H}(\boldsymbol{\sigma}, e, \dot{\varepsilon})$ where, $\dot{\sigma}$ is the Zareba-Jaumann stress rate, e denotes the void ratio and $\dot{\varepsilon}$ is the strain rate tensor. The general form of the tensorial function $\boldsymbol{H}$ is selected such that

$$\dot{\sigma} = \mathbf{L}\dot{\varepsilon} + \mathbf{N}\|\dot{\varepsilon}\|, \tag{13}$$

where, L and are fourth-order linear and second-order non-linear constitutive tensors respectively, with $\|\dot{\varepsilon}\|$ denoting the Euclidean norm of the strain rate tensor. In the hypoplasticity formulation, the solid-state is characterized by three values of void ratio, given by the relation,

$$\frac{e_i}{e_{i0}} = \frac{e_c}{e_{c0}} = \frac{e_d}{e_{d0}} = exp\left[-\left(\frac{tr\,\sigma}{h_s}\right)^n\right], \tag{14}$$

where, e_i is the maximum possible void ratio, e_c the critical void ratio, e_d the minimum void ratio, h_s the pressure independent granular stiffness and n is an input index. The subscript 0 indicates a reference value. For cyclic load applications, the intergranular strain concept takes into account the elastic deformation. If the strain is within the limit of intergranular strain, the small strain stiffness is invoked; else the basic hypoplastic model is activated.

5. Convected particle domain Interpolation method

The advantage of Convected Particle Domain Interpolation Method (*CPDI*) over *MPM* is its ability to mitigate cell-crossing noise. This error is particularly noticeable when using linear basis functions, which most *MPM* formulations employ. As a consequence of using linear shape function, the gradient is discontinuous between cells, causing a jump in the local internal forces as a particle crosses a grid boundary. By defining a finite size domain, such as that used in Generalized Interpolation Material Point Method (*GIMP*) (Bardenhagen and Kober, 2004), *uGIMP* (Wallstedt and Guilkey, 2008), or *CPDI*, the cell-crossing noise is reduced.

As opposed to the conventional *MPM*, in which the particle domains are collocated, the *CPDI* method describes a particle's domain by two vectors $(\boldsymbol{r}_1^0, \boldsymbol{r}_2^0)$, in which the superscript 0 depicts the current initial state, and subscripts 1 and 2 refer to the vectors in the horizontal and vertical directions. As a particle moves during the course of a simulation, its domain is allowed to deform according to relations:

$$\boldsymbol{r}_1^n = \boldsymbol{F}_p^n \cdot \boldsymbol{r}_1^0, \quad \boldsymbol{r}_2^n = \boldsymbol{F}_p^n \cdot \boldsymbol{r}_2^0, \tag{15}$$

where, n refers to the updated time step and $\boldsymbol{F}_p^n$ is the updated deformation gradient.

To eliminate the requirement of having to divide the particles according to cell boundaries, *CPDI* introduces an alternative set of basis functions that are defined according to the domain of each particle (Sadeghirad et al., 2011); i.e.,

$$\phi_{ip} \cong \frac{1}{4}[S_i(\boldsymbol{x}_1^p) + S_i(\boldsymbol{x}_2^p) + S_i(\boldsymbol{x}_3^p) + S_i(\boldsymbol{x}_4^p)], \tag{16}$$

in which $S_i(\boldsymbol{x}_j^p)$ represents the grid basis functions with $j \in [1, 2, 3, 4]$ referring to the corners of particle p domain. The deformation gradient $\boldsymbol{F}_p^n$ is updated according to the relation:

$$\boldsymbol{F}_p^{n+1} = (I + \nabla \boldsymbol{v}_p^{n+1}\Delta t)\boldsymbol{F}_p^n, \tag{17}$$

where, Δt is the incremental time step, $\boldsymbol{I}$ is a second-order identity tensor.

6. Contact algorithm

MPM provides an automatic no-slip, no-separation, contact algorithm that prevents interpenetration of two entities when in contact. Early research focused on relaxing the no-slip and no-separation condition (Bardenhagen et al., 2001). The applicability of the different interaction schemes to couple FE schemes with fluids or solid formulated in the framework of Material Point Method is addressed in (Hamad et al., 2015; Hamad et al., 2016). The contact algorithm adopted in Reference (Hamad et al., 2017) was shown to be more stable and accurate than the traditional *MPM* contact algorithm. It is based on penalizing the potential energy proportionally to the amount of constraint violation by using a penalty function P, expressed as:

$$P = \frac{1}{2}\omega_n \int_{\Gamma_c} g_n^2 \, d\Gamma_c + \frac{1}{2}\omega_t \int_{\Gamma_c} g_t^2 \, d\Gamma_c, \tag{18}$$

in which, ω is the penalty parameter, g represents gap functions, with subscripts n and t corresponding to the normal and tangential directions, respectively. In this method, the interface of a continuum is discretized using two-node linear segments. The normal and tangential stiffness, which are the penalty parameters, are assigned to these elements. A distinction between master and slave is made in the formulation for numerical convenience. A detailed description of the formulation is presented in (Hamad et al., 2017).

7. Shake table test example

To alleviate concerns regarding the liquefaction susceptibility of large embankment dams, centrifuge tests were commissioned to investigate the behavior of saturated soils under high confining stresses encountered in deep deposits (Gonzalez et al., 2002). Numerical modeling of shake table shown in Fig. 1 was completed by Byrne and coworkers

(Byrne et al., 2004) using FLAC together with UBCSAND. The column was subjected to a 'vertical'- centrifugal acceleration of 120g together with cyclical horizontal load of 0.2g at 1.5 *Hz*.

The numerical model corresponding to 1 g prototype that was utilized for the current study is also depicted in Fig. 1. It consisted of 38 m high uniform, saturated Nevada sand, which was assumed to have an initial relative density of $D_r = 55\%$. The horizontal loading used for the centrifuge study was also adopted for the numerical model. Table 1 summarizes the parameters used for the simulations. While the first two rows of parameters were defined previously in terms of well-known properties, the third row consists of calibration parameters that fine-tune the stress–strain details.

The *CPDI* models of the prototype had 468 background grid elements together with 3429 particles. The goal of this simulation was to verify if a one-dimensional representation could accurately capture the experiment. Particles on left- and right-boundaries were "tied together", to enforce simple shear and by extension, uniform pressure and effective stresses along each horizontal layer of particles. The volumetric strains could only develop due to vertical strains.

The acceleration effects at the base of the column were applied to the particles via d'Alembert's principle. A forward-Euler time-stepping algorithm was adopted to integrate the momentum equations with a nominal 1% Particle-in-Cell damping (Nairn, 2015) being provided when calculating the particle velocities of both phases. Unlike in Reference (Byrne et al., 2004), interface elements were not implemented to account for potential silo effects that develop as the consequence of the soil interacting with the walls of container.

The predicted effective stress variation with depth, which shows the reduction of mean effective stress, at different times, are presented in Fig. 2. Since the effective stresses were not logged during the experiment, the predictions from the numerical simulation provide an insight into the development of effective stresses in the column during the course of simulation. It should be noted that a reduction in recorded stress rate at different heights of the column, which was observed (Gonzalez et al., 2002, Byrne et al., 2004) experimentally, was captured by the numerical model. The top-down liquefaction trend, reported in (Gonzalez et al., 2002) was also predicted by the *CPDI* model. Numerical instabilities developed at the top of the column near the end of the simulation when the effective stresses were close to zero. It can be argued that, because the increase in pore pressures was directly related to the drop in effective stresses, it is reasonable to conclude that the predictions were in agreement with what had been observed experimentally.

Plotting the predictions of excess pore pressure evolution in Fig. 3 at different heights sheds light on the *CPDI*'s capability to reproduce the rate of liquefaction when compared to the experimental results presented in (Byrne et al., 2004). Fig. 3 shows that the maximum predicted excess pore pressure from the numerical solution is less than what

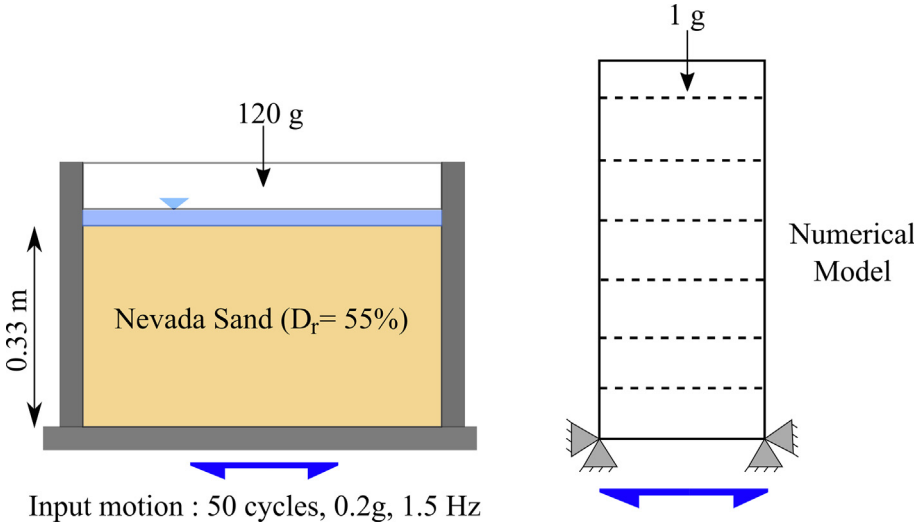

Fig. 1. Schematic of experimental and numerical setup of shake table test, performed at the Rensselaer Polytechnic Institute.

Table 1
UBCSAND model parameters for Nevada Sand.

$N1_{60}[-]$	$m_e[-]$	$n_e[-]$	$n_p[-]$	$K^e_G[-]$	$K^e_B[-]$
10.7	0.5	0.5	0.5	800	1100
$K^p_G[-]$	$\phi_{pt}[^\circ]$	$\phi_f[^\circ]$	$c[kPa]$	$Pa[kPa]$	$\sigma_t[kPa]$
500	31	32	0	100	0
$hfac_1[-]$	$hfac_2[-]$	$hfac_3[-]$	$hfac_4[-]$	$hfac_5[-]$	$hfac_6[-]$
0.3	0.85	1.0	0.6	1.0	0.95

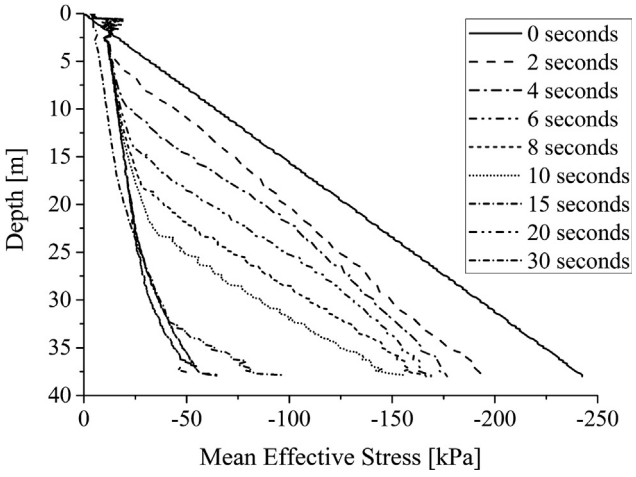

Fig. 2. Mean effective stresses throughout the column at different stages.

had been observed in the experimental study. This is consistent with the fact that the effective stresses did not drop all the way to zero in these regions. This difference can likely be corrected by better calibrating the parameters to obtain a closer fit to the experimental values.

We observe, for example, in Fig. 3 that the simulated rate of generation of excess pore pressure corresponding to a height of 13.2 m, is initially close to what had been recorded in experiment until 2.5 s. The rate of generation of excess pore pressures starts to deviate thereafter when compared with the experiment, yielding a lower than measured final excess pore pressure. In addition to the predicted excess pore pressures being different, the predicted times at which the excess pore pressures stayed constant tended to be different. At a height of 1 m, the predictions indicated a more rapid increase to a constant pore pressure than what was observed experimentally. The slight oscillations in pore pressure indicate that the effective stresses were not zero. The reasoning behind this being that the pore pressures were calculated as a contribution of fluid strains and mixture strains, i.e., changes in mixture strains arose as a consequence of the change in pore pressures and effective stress. The comparisons in this section demonstrate nevertheless that the two-phase *CPDI* method incorporating the UBCSAND model was capable of capturing the liquefaction development to a reasonable degree of accuracy, although differences are apparent.

Fig. 3 shows that the *CPDI* model predicts the excess pore pressure that are slightly lower. Thus, the dependence of excess pore pressure on hydraulic conductivity was studied using a 1-D, 38-element finite element model of the shake table test. Once again, the UBCSAND model with Nevada sand parameters were adopted.

The 1-D model, which avoids wave reflections from vertical boundaries are described by equations:

$$\frac{\partial \sigma_{xy}}{\partial y} + \rho \frac{\partial u_{base}}{\partial t} = \rho \frac{\partial u}{\partial t}, \tag{19}$$

$$\frac{\partial \sigma'_{yy}}{\partial y} + \rho' g = \bar{\rho} \frac{\partial v}{\partial t} + \frac{\rho_w g}{k} v, \tag{20}$$

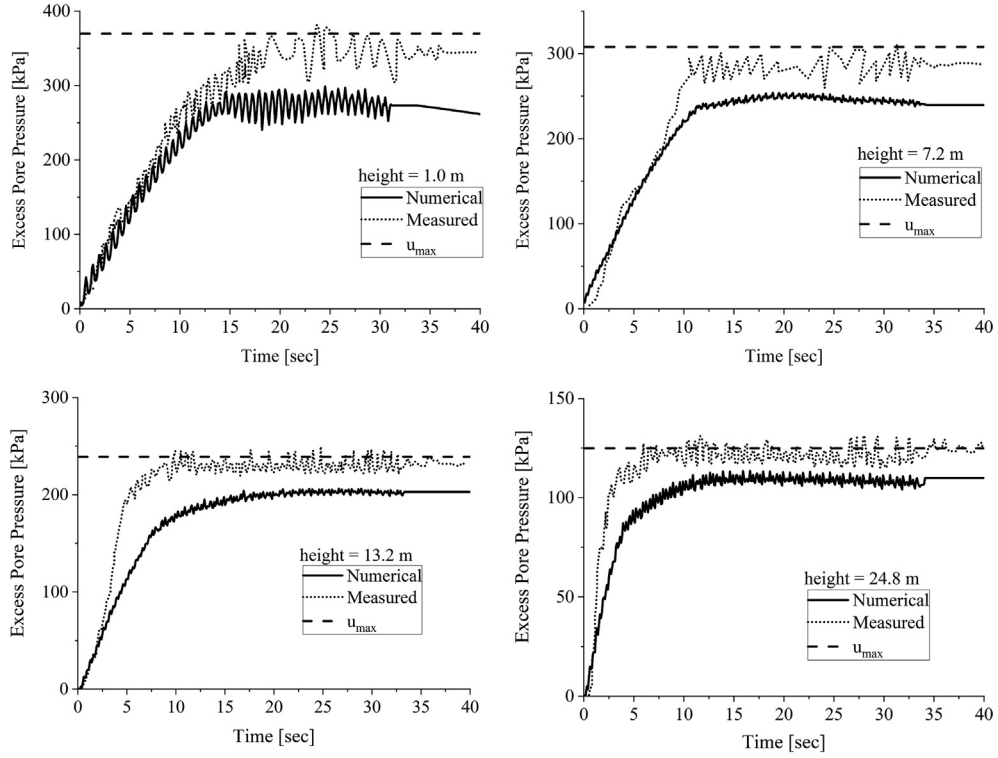

Fig. 3. Evolution of Excess Pore Pressure at heights 1 m, 7.2 m, 13.2 m and 24.8 *m*.

where σ_{xy} is the shear stress, $\frac{\partial u_{base}}{\partial t}$ is the acceleration of the base, u and v are velocities in $x-$ and $y-$ directions, respectively. k is the hydraulic conductivity. ρ and ρ_w are the mixture and water unit weights, respectively. $\bar{\rho}$ is given by the relation $\bar{\rho} = \rho' + \frac{\rho}{n}$, buoyant unit weight ρ' being given by $\rho' = \rho - \rho_w$, and n is the porosity. These differential equations are obtained assuming full incompressibility $(1-n)\ \frac{\partial v}{\partial y} + n\ \frac{\partial w}{\partial y} = 0$, where w represents the velocity of the water. It should be noted that this model does not suffer from presence of vertical boundaries. Therefore, there is no need to consider wave reflections from the vertical boundary.

Fig. 4, which shows the excess pore pressure development normalized with respect to the initial effective stress, clearly shows that the salient features of excess pore pressure generation are captured for $k = 0.001$ m/s and 0.000121 m/s. At a height of 25 m, we observe that the excess pore pressure at the lower k-value, leads to liquefaction sooner, whereas at the higher value we observe that the generated excess pore pressure levels off before liquefaction is eventually reached. Near the bottom, liquefaction occurs for both permeabilities, which is what one might expect given the length of the drainage path. The cyclic variation in pore pressure at the bottom reflects the loading–unloading sequences. The more rapid development of pore pressure for the 1-D model compared to the *CPDI* model is attributed to the stronger enforcement of incompressibility. Given these results, the predicted lower excess pore pressures are consistent with what is observed in Fig. 3.

Similar analyses assuming UBCSAND and Nevada sand parameters had been completed with a two-dimensional 38 element model to get an idea of the computational time with different hydraulic conductivities. For $k = 0.001$ m/s, it took approximately 12 min for the calculation, while for $k = 0.000121$ m/s, it took 55 min. The higher values were selected to reduce computational time. The relation between hydraulic conductivity and time-step is provided in Reference (Mieremet et al., 2016).

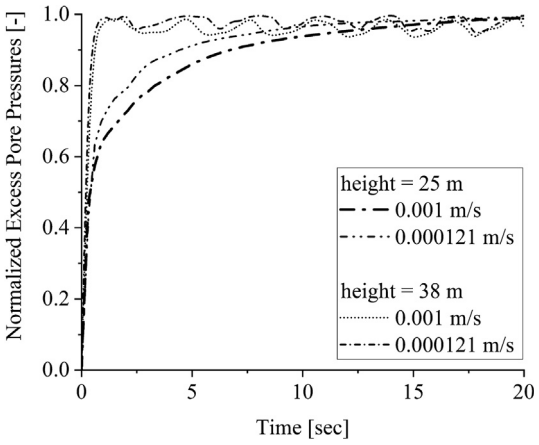

Fig. 4. Parameter study: Hydraulic conductivity.

It should be highlighted at this point that the *CPDI* predictions of the shake table prototype correspond to a one-dimensional situation as did those reported in (Byrne et al., 2004). In actual fact, the experimental setup was a two-dimensional problem. The conditions at the walls of the sand container were not taken into account as indicated previously and the assumption of uniform properties may be too strong, even though extreme care was likely taken when fabricating the physical test specimen. Therefore, some differences between measurements and predictions should be expected. What is important here is that the overall characteristics were captured.

8. Comparing the UBCSAND model and Hypoplastic soil models

Simulations for the shake-table test described previously were performed using the properties of Berlin sand to draw a comparison between the predictions of the UBCSAND and *HPS* soil models for a boundary-valued problem in which the boundary and loading conditions were well-defined. The boundary and the loading conditions, as well as the number of particles and the background grid, remained unchanged. For this case, the particle-in-cell damping, which was previously 1%, was set to 2%. This increase in damping value was necessary purely for numerical stability reasons. The properties of Berlin sand were adopted given that the parameters for Berlin sand existed for the HPS model and high-quality experimental data were available to calibrate the UBCSAND sand model. Besides, Berlin sand was used in the experimental study that is presented in the section that follows.

The monotonic and cyclic test data obtained from the work of (Le, 2015), which corresponded to a relative density Dr = 75%, were used to calibrate the constitutive models. The calibration for the UBCSAND model used the procedure presented in (Shriro and Bray, 2013) to estimate the reference values for the stiffness parameters and stress exponents. These values were later refined via an iterative process to obtain a better fit to the published results. Tables 2 and 3 provides the constitutive parameters for UBCSAND and HPS model for Berlin sand, respectively, with the physical properties for both being presented in Table 4. It should be noted that the Berlin sand is coarser than Nevada sand.

Fig. 5 compares the cyclically induced evolution of mean effective stress at heights of 13.2 m and 24.8 m over time with each constitutive model. It is clear that the top-down liquefaction developed as the mean effective stress approached zero and plateaued near the top of the column before plateauing below 13.2 m. This behavior is consistent with the results shown in Fig. 3 that were experimentally observed during the test with Nevada sand. It is clear that the predicted rates at which the soil loses strength along the upper part of the column (24.8 m) is nearly identical for both constitutive models. The average rate of liquefaction associated with the HPS model is higher than that of the

UBCSAND model; i.e., the development of effective stress plateaus sooner. The final strength of the soil predicted by each model during post-liquefaction is slightly different, with the HPS model predicting less strength when compared with that of the UBCSAND model. For both cases, we observe incomplete liquefaction. The results here are similar to what was predicted with the UBCSAND model when using the Nevada sand soil parameters.

Fig. 6 presents the evolution of excess pore pressure. Here again, it is observed that in the top portion of the column (24.8 m), the rate of evolution of excess pore pressure is comparable; although one could discern that the average rate of evolution of excess pore pressure in the case of HPS model is slightly higher than that of the UBCSAND model. The behavior of the bottom portion of the section is similar to what can be discerned by examining the evolution of mean effective stresses, as might be expected. By and large, the comparison of predictions is reasonably good.

Comparing the results of the excess pore pressures between Nevada and Berlin sand shown in Fig. 7, we can observe that the rates of pressure increase captured numerically given the same permeability is initially approximately equal for both sands. The times at which the values plateau is also approximately the same, but the peak values that the models attain are vastly different for the models. Incomplete liquefaction is observed in both models, consistent with what was explained previously. This difference in results is not surprising as the parameters chosen for Berlin sand correspond to a denser soil than those chosen for Nevada sand, with the initial void ratio for Nevada and Berlin sands being 0.68 and 0.465, respectively. This result is consistent with the work of (Vaid et al., 1990), where it is reported that poorly graded soils ($C_u < 6$) and soils at lower relative densities (in this case Nevada sand) are found to have a lower cyclic strength. The opposite trend was observed at higher relative densities (in this case Berlin sand).

Table 4
Physical properties of Nevada and Berlin Sand.

Parameter	Nevada Sand	Berlin Sand
$G_s[-]$	2.67	2.61
$e_0[-]$	0.68	0.465
$e_{min}[-]$	0.511	0.391
$e_{max}[-]$	0.877	0.688
$D_{10}[mm]$	0.11	0.20
$D_{50}[mm]$	0.17	0.55
$C_u[-]$	1.75	3.25
$C_c[-]$	0.88	0.60

9. Comparison of predictions using both UBCSAND and Hypoplastic soil models for pile installation

It is known that during the vibratory installation of a pile an increase in pore water pressure develops in a zone around the pile. This has been documented for example in the work of (Mabsout et al., 1995, Pestana et al., 2002, Mahutka et al., 2006), among others. Thus, the possibility of liquefaction development cannot be ignored. Although one can model the development of excess pore pressure when employing a coupled formulation, the accuracy of the magnitude of generated excess pore pressure and the subsequent reduction in effective stresses are very much at the mercy of the constitutive model adopted for the soil. Reference (Schümann and Grabe, 2011) implemented a multi-phase formulation that incorporated the HPS model (Von Wolffersdorff, 1996) using ABAQUS to model the phenomenon. The excess pore pressures were captured in their analysis along with the corresponding reduction in effective stress around the pile. Reference (Osinov et al., 2013) presented a finite element analysis that simulated a vibratory-driven pile. Their analyses managed to simulate a liquefaction zone around the pile, once again adopting a HPS model.

Table 2
UBCSAND model parameters for Berlin Sand.

$N1_{60}[-]$	$m_e[-]$	$n_e[-]$	$n_p[-]$	$K^e_G[-]$	$K^e_B[-]$
11.5	0.5	0.5	0.4	1224	1120
$K^p_G[-]$	$\phi_{pt}[^\circ]$	$\phi_f[^\circ]$	$c[kPa]$	$Pa[kPa]$	$\sigma_t[kPa]$
423	31.5	37.5	0	100	0
$hfac_1[-]$	$hfac_2[-]$	$hfac_3[-]$	$hfac_4[-]$	$hfac_5[-]$	$hfac_6[-]$
0.65	0.85	1.0	0.6	1.0	0.95

Table 3
Hypoplastic model parameters for Berlin Sand.

$\phi_c[^\circ]$	$p_t[-]$	$h_s[MPa]$	$n[-]$	$e_{d0}[-]$
31.5	–	230e6	0.3	0.391
$e_{c0}[-]$	$e_{i0}[-]$	$\alpha[-]$	$\beta[-]$	$m_R[-]$
0.688	0.791	0.13	1	4.4
$m_T[-]$	$R[-]$	$\beta_r[-]$	$\chi[-]$	$e_0[-]$
2.2	$1e-4$	0.2	6	–

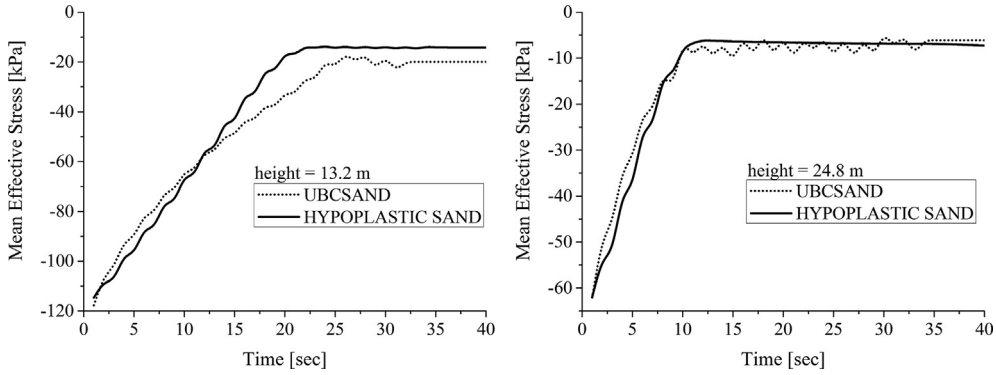

Fig. 5. CPDI simulation of shake table test: Comparison of the mean effective stress for both models at heights 13.2 m and 24.8 *m*.

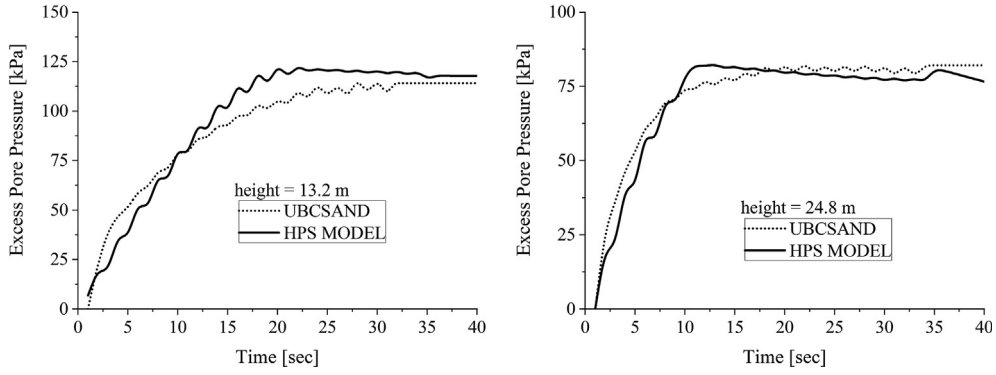

Fig. 6. Comparison of the excess pore pressures for both models at heights 13.2 m and 24.8 *m*.

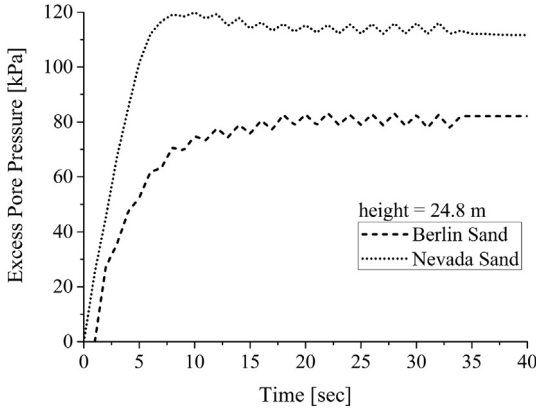

Fig. 7. Comparison of Nevada and Berlin sand using the UBCSAND model; Excess Pore Pressure at a height 24.8 *m*.

Building upon this knowledge, an axially-symmetric *CPDI* formulation, based on the work of (Hamad, 2016) along with the penalty contact procedure elaborated in detail in (Hamad et al., 2017), was adopted to model a pile installation. The predictions were compared against published experimental data for a scaled model test. A detailed explanation of the test setup used and the testing scheme is presented in the work of (Remspecher et al., 2018). A multi-phase *CPDI* model was utilized in the current study, along with the HPS and UBCSAND sand models. The objective was to model the pore pressure evolution and compare predictions to measured values at one control point.

Definition of problem - A model-scale hollow pile with a diameter of 0.2 m was vibrated into a soil that was assumed to be homogeneous and fully saturated. Initial stresses were assumed to correspond to K_0 conditions ($K_0 = 0.5$). The *CPDI* model was allowed to reach steady-state before the application of a harmonic load. The frequency of the load that was applied directly to the pile head was 23 *Hz*. The bulk modulus of water (K_f) was taken as 2.2 GPa. Such a high value imposed a considerable computational overhead due to the explicit time-stepping scheme that was adopted. In the work of (Osinov et al., 2013), it is shown that by reducing the bulk modulus of water by a factor of 10, a higher effective stress state for the zone of liquefaction is observed. For this reason, a more accurate value was adopted to provide more realistic conditions. The pile was assumed to vibrate only in the vertical direction, with the horizontal movement of the pile being restricted. Interface elements, which served to model contact between the pile and the soil assumed a friction coefficient (μ) value of 0.38.

The axially-symmetric boundary shown in Fig. 8 was discretized with approximately 25,000 particles representing the soil and pile domain, along with 1,500 interface elements. The figure shows that an irregular meshing scheme was utilized in which more particles were packed near the toe and the jacket of the pile. Thus the dynamics of

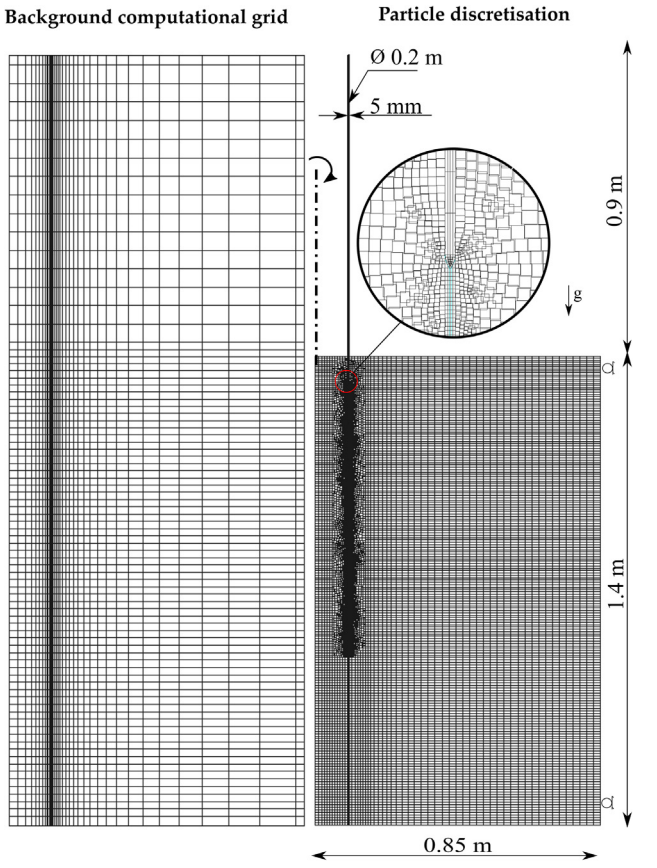

Fig. 8. Background computational grid discretisation (Left) and Particle discretisation of soil and pile (Right).

the process and faster a convergence of the solution could be realized. The pile was initially embedded 0.1 m, which approximated the pile penetration due to gravity that was observed in the experiment. A continuously updated time-stepping scheme was implemented, in which the time step was updated according to the continuously evolving stiffness parameter every 100-time steps. Particle-in-cell damping, as introduced in the previous section, was assigned as 1% for both the solid and fluid phases. Both HPS and UBCSAND models were adopted using the parameters shown in Tables 2 and 3, respectively, in which a relative density of 75% was assumed for both constitutive models.

Results - Referring to Fig. 9, a reasonable match between the experiment and the numerical predictions are observed with both constitutive laws. The constitutive models together with the *CPDI* multi-phase formulation were capable of reproducing the measured installation depth over time quite well. Both *HPS* and *UBCSAND* models captured the initial relatively high rate of installation and the gradual decrease in the rate of penetration, a phenomenon that is attributed to factors such as the increase in skin friction acting along the length of the shaft.

Fig. 10 presents the predicted effective radial stresses in the soil with depth at a radius of 1 cm from the axis of rotation (inside the pile) and 12 cm from the axis (outside the pile), corresponding to a pile penetration of 47 cm. The

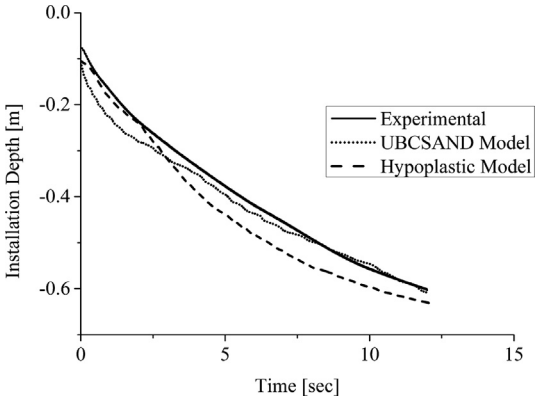

Fig. 9. Vertical penetration of the pile - Experiment vs. Numerical.

simulations were started from the geostatic stress state. As the vibration commenced, an increase in effective radial stress was observed, which is attributed to the dynamic action of the pile on the soil skeleton. For the case of the HPS model, a maximum increase of 20 kPa is estimated inside the pile and a slightly larger value outside the pile. The region of maximum stress is seen to correspond to the position of the pile foot. As might be expected, the radial stresses exceed the K_0 values.

During the vibration process, high stresses were observed under the tip of the pile, with a zone of elevated stress corresponding 3*D* to 4*D* around the location of the pile. This result is in good agreement with the work of (Mahutka et al., 2006), who had calculated a similar response. Referring to Fig. 10, the same elevated stress response is observed outside the pile as well. For the case of the UBCSAND predictions, a similar trend is observed, both inside and outside the pile, but the magnitude of the effective radial stress is much larger than that corresponding to K_0 conditions. This may be attributed to the fact that the HPS model takes into account void ratio changes. The stress distribution below the pile eventually followed the geostatic distribution.

Fig. 11 compares the excess pore pressure evolution for the numerical and the experimental results corresponding to a depth of 35 cm from the top of the soil at a distance of 2 cm away from the pile. Starting from a hydrostatic pressure distribution, one observes a build-up of excess pore pressure. Negative values indicate excess pore pressure development with positive values noting suction. It can also be observed that both the HPS and UBCSAND models can replicate the trend of excess pore pressure generation for approximately 5 s of vibration, which corresponds to an installation depth of 35 cm (see Fig. 9), the results during the first 5 s are however markedly different. The models also capture the suction that is observed to develop in the region after the pile toe has passed the control level. Both simulations and the measurements confirm that an excess of pore pressure develops until the pile tip reaches the control point, beyond which it shifts to the suction regime. While the UBCSAND model is capable of nicely capturing the excess pore pressure development, oscillations in the values of the

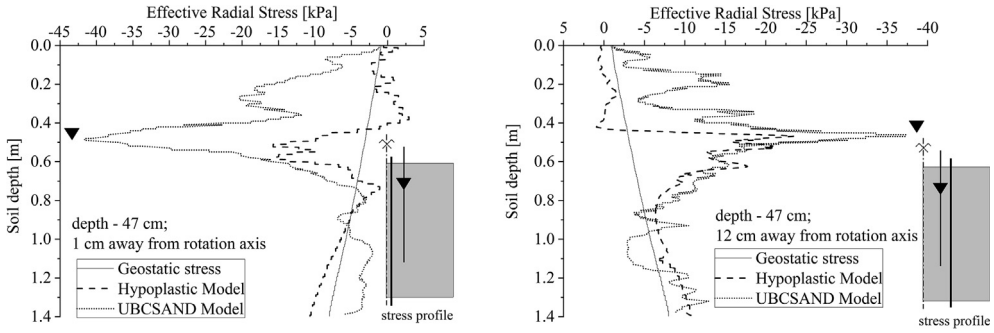

Fig. 10. Effective stress distribution inside (Left) and outside (Right) the pile - HPS and UBCSAND models.

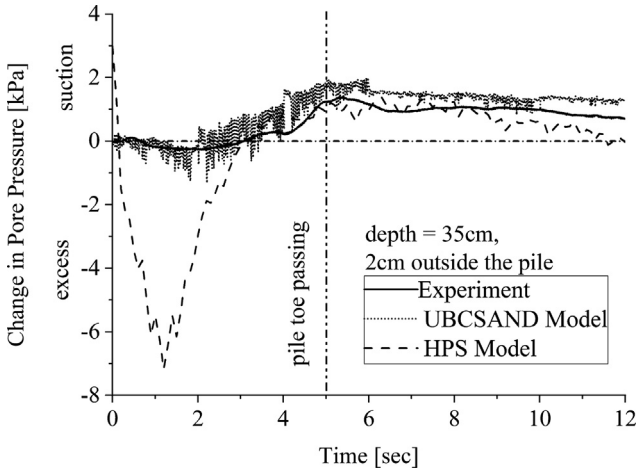

Fig. 11. Pore pressure development - HPS and UBCSAND models compared against experiment.

pore pressure are observed. More investigations are necessary to ascertain as to why the HPS model predicts a −7 kPa spike in excess pore pressure at approximately 3 s compared with a measured value of −0.5 kPa. At this stage, it is theorised that it is a numerical artefact from the *MPM* code. It should be noted that a state of total liquefaction is not observed, which implies that the effective stresses do not fully vanish.

10. Remarks on computational time

This study demonstrated that the responses of UBCSAND and HPS model are similar. One must, however, answer the question, what advantage does one model provide over the other. Having seen that the responses of both models are comparable, we can now start reliably using the model with lower computational cost over the one that has a higher computational cost if the goal is not a comprehensive simulation of the stress and soil state, but rather is to estimate the penetration depth and pore pressure. It should be appreciated that for a similar response, the computational time for the UBCSAND is considerably lower than that for the HPS model. The UBCSAND model took 62 h to simulate 12 s of pile vibration, whereas the HPS model required 96 h. While both models were run on Intel Xeon family of Workstation processors with comparable clockspeeds, the UBCSAND model utilized 16 threads, whereas the HPS model 20 threads. Here, UBCSAND model can be reliably substituted in lieu of HPS model, in the context of *CPDI* for pile installation simulation.

11. Concluding remarks

The UBCSAND model (Naesgaard, 2011) was implemented in the *CPDI* code that included the effects of solid and fluid phases via a single particle, $v - w$ formulation. The properties for the UBCSAND were calibrated against published data for Nevada and Berlin sand. The benchmark tests were performed using the multi-phase *CPDI* and UBCSAND model and the results were compared against published experimental results, as well as results obtained incorporating the hypoplasticity model.

The objective of the paper was to present a numerical framework capable of simulating large deformation as a consequence of liquefaction. The emphasis in this preliminary study was to systematically accommodate the physics of water-particle interaction, including possible liquefaction, for real-life processes including pile installation with the knowledge that this method has been previously applied to problems involving large deformations (Moormann and Hamad, 2015, Bhandari et al., 2016, Hamad, 2016). The tool developed in this work serves as a base on which further large deformation problems involving liquefaction can be developed. Subsequent improvements to the analyses, particularly for simulating the shake table test, will include the addition of interface elements to accommodate the silo effect and to model the two-dimensional nature of the problem.

Acknowledgements

A portion of the research leading to results presented in the paper was partly funded under the framework of the project ‘CAFE - Cyclic and Near Field Effects of Vibratory Driving in Sand´. The authors would like to acknowledge the funding of innogy SE.

References

Bardenhagen, S.G., Kober, E.M., 2004. The generalized interpolation material point method. Computer Modeling in Engineering and Sciences 5, 477–496.

Bardenhagen, S.G., Guilkey, J.E., Roessig, K.M., Brackbill, J.U., Witzel, W.M., Foster, J.C., 2001. An improved contact algorithm for the material point method and application to stress propagation in granular material. Computer Modeling in Engineering and Sciences 2, 509–522.

Berrill, J.B., Davis, R.O., 1985. Energy dissipation and seismic liquefaction of sands: revised model. Soils Found. 25, 106–118.

Bhandari, T., Hamad, F., Moormann, C., Sharma, K.G., Westrich, B., 2016. Numerical modelling of seismic slope failure using MPM. Comput. Geotech. 75, 126–134.

Byrne, P.M., Park, S.-S., Beaty, M., Sharp, M., Gonzalez, L., Abdoun, T., 2004. Numerical modeling of liquefaction and comparison with centrifuge tests. Can. Geotech. J. 41, 193–211.

Giridharan, S., Stolle, D., & Moormann, C. (2019). Modelling liquefaction using the Material Point Method – an evaluation using two constitutive models. 2nd International Conference on the Material Point Method for Modelling Soil-Water-Structure Interaction, 8-10 January 2019 Churchill College, Cambridge, United Kingdom, 82-89.

Gonzalez, L., Abdoun, T., Sharp, M.K., 2002. Modelling of seismically induced liquefaction under high confining stress. International Journal of Physical Modelling in Geotechnics 2, 1–15.

Hamad, F., 2016. Formulation of the axisymmetric CPDI with application to pile driving in sand. Comput. Geotech. 74, 141–150.

Hamad, F., Giridharan, S., Moormann, C., 2017. A penalty function method for modelling frictional contact in MPM. Procedia Eng. 175, 116–123.

Hamad, F., Stolle, D., Moormann, C., 2016. Material point modelling of releasing geocontainers from a barge. Geotext. Geomembr. 44, 308–318.

Hamad, F., Stolle, D., Vermeer, P., 2015. Modelling of membranes in the material point method with applications. Int. J. Numer. Anal. Meth. Geomech. 39, 833–853.

Hleibieh, J., Wegener, D., Herle, I., 2014. Numerical simulation of a tunnel surrounded by sand under earthquake using a hypoplastic model. Acta Geotech. 9, 631–640.

Juang, C.H., Chen, C.J., Jiang, T., 2001. Probabilistic framework for liquefaction potential by shear wave velocity. J. Geotech. Geoenviron. Eng. 127, 670–678.

Le, V. H. (2015). Zum Verhalten von Sand unter zyklischer Beanspruchung mit Polarisationswechsel im Einfachscherversuch. Technische Universität Berlin. Shaker Verlag.

Mabsout, M.E., Reese, L.C., Tassoulas, J.L., 1995. Study of pile driving by finite-element method. Journal of Geotechnical Engineering 121, 535–543.

Mahutka, K. P., König, F., & Grabe, J. (2006). Numerical modelling of pile jacking, driving and vibratory driving. Proceedings of International Conference on Numerical Simulation of Construction Processes in Geotechnical Engineering for Urban Environment (NSC06), Bochum, ed. T. Triantafyllidis, Balkema, Rotterdam, (S. 235-246).

Mieremet, M.M., Stolle, D.F., Ceccato, F., Vuik, C., 2016. Numerical stability for modelling of dynamic two-phase interaction. Int. J. Numer. Anal. Meth. Geomech. 40, 1284–1294.

Moormann, C., Hamad, F., 2015. MPM dynamic simulation of a seismically induced sliding mass. IOP Conference Series: Earth and Environmental Science 26 012024.

Moormann, C., Gowda, S., Giridharan, S., 2018. Numerical simulation of pile installation in saturated soil using CPDI. Proceedings of the 9th European Conference on Numerical Methods in Geotechnical Engineering, pp. 665–672.

Naesgaard, E. (2011). A hybrid effective stress–total stress procedure for analyzing soil embankments subjected to potential liquefaction and flow. Ph.D. dissertation, University of British Columbia.

Nagula, S., Grabe, J., 2017. 2-Phase dynamic simulation of deep sand compaction to reduce liquefaction. Procedia Eng. 199, 2396–2401.

Nairn, J.A., 2015. Numerical simulation of orthogonal cutting using the material point method. Eng. Fract. Mech. 149, 262–275.

Niemunis, A., Herle, I., 1997. Hypoplastic model for cohesionless soils with elastic strain range. Mechanics of Cohesive-frictional Materials: An International Journal on Experiments, Modelling and Computation of Materials and Structures 2, 279–299.

Osinov, V.A., Chrisopoulos, S., Triantafyllidis, T., 2013. Numerical study of the deformation of saturated soil in the vicinity of a vibrating pile. Acta Geotech. 8, 439–446.

Pestana, J.M., Hunt, C.E., Bray, J.D., 2002. Soil deformation and excess pore pressure field around a closed-ended pile. J. Geotech. Geoenviron. Eng. 128, 1–12.

Puebla, H., 1999. A constitutive model for sand and the analysis of the CanLex Embankments Ph.D. dissertation. University of British Columbia.

Puebla, H., Byrne, P.M., Phillips, R., 1997. Analysis of CANLEX liquefaction embankments: prototype and centrifuge models. Can. Geotech. J. 34, 641–657.

Remspecher, F., Le, V.H., Rackwitz, F., Herwig, V., Matlock, B., 2018. Vibratory Driven Installation of Monopiles–An Experimental Investigation of the Soil-Pile Interaction. Vietnam Symposium on Advances in Offshore Engineering, pp. 171–176.

Robertson, P.K., Wride, C.E., 1998. Evaluating cyclic liquefaction potential using the cone penetration test. Can. Geotech. J. 35, 442–459.

Sadeghirad, A., Brannon, R.M., Burghardt, J., 2011. A convected particle domain interpolation technique to extend applicability of the material point method for problems involving massive deformations. Int. J. Numer. Meth. Eng. 86, 1435–1456.

Schümann, B., Grabe, J., 2011. FE-based modelling of pile driving in saturated soils. Proceedings of the 8th International Conference on Structural Dynamics, pp. 894–900.

Shriro, M., Bray, J.D., 2013. Calibration of Numerical Model for Liquefaction-Induced Effects on Levees and Embankments. Missouri University of Science and Technology.

Tsegaye, A.B., Molenkamp, F., Brinkgreve, R.B., Bonnier, P.G., Jager, R., Galavi, V., 2010. Modeling liquefaction behaviour of sands by means of hypoplastic model. 7th European Confrerence on Numerical Methods in Geotechnical Engineering, pp. 81–87.

Vaid, Y.P., Fisher, J.M., Kuerbis, R.H., Negussey, D., 1990. Particle gradation and liquefaction. Journal of Geotechnical Engineering 116, 698–703.

Van Esch, J., Stolle, D., Jassim, I., 2011. Finite element method for coupled dynamic flow-deformation simulation. 2nd International Symposium on Computational Geomechanics (COMGEO II).

Von Wolffersdorff, P.-A., 1996. A hypoplastic relation for granular materials with a predefined limit state surface. Mechanics of Cohesive-frictional Materials: An International Journal on Experiments, Modelling and Computation of Materials and Structures 1, 251–271.

Wallstedt, P.C., Guilkey, J.E., 2008. An evaluation of explicit time integration schemes for use with the generalized interpolation material point method. J. Comput. Phys. 227, 9628–9642.

Zienkiewicz, O.C., Shiomi, T., 1984. Dynamic behaviour of saturated porous media; the generalized Biot formulation and its numerical solution. Int. J. Numer. Anal. Meth. Geomech. 8, 71–96.

Zienkiewicz, O. C., Chan, A. H., Pastor, M., Paul, D. K., & Shiomi, T. (1990). Static and dynamic behaviour of soils: a rational approach to quantitative solutions. I. Fully saturated problems. In: Proceedings of the Royal Society of London. A. Mathematical and Physical Sciences, 429, 285-309.